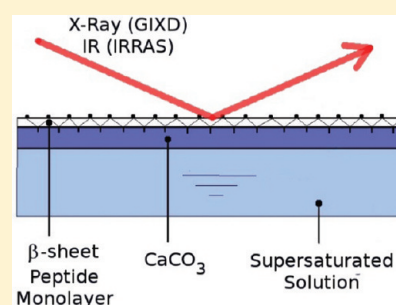


CaCO<sub>3</sub> Mineralization under  $\beta$ -Sheet Forming Peptide MonolayersNicolas R. Chevalier,<sup>†</sup> Corinne Chevillard,<sup>†</sup> Michel Goldmann,<sup>‡</sup> Gerald Brezesinski,<sup>§</sup>  
and Patrick Guenoun<sup>\*,†</sup><sup>†</sup>DSM, IRAMIS, LIONS, UMR CEA-CNRS 3299, CEA-SACLAY 91191 Gif-sur-Yvette cedex, France<sup>‡</sup>Institut des Nanosciences de Paris, Université Pierre et Marie Curie, 2 Place Jussieu, 75252 Paris cedex 05, France, and Université Paris Descartes, 45 rue des Saints-Pères, 75270 Paris cedex 06, France<sup>§</sup>Max Planck Institute of Colloids and Interfaces, Science Park Golm, 14476 Potsdam, Germany

## Supporting Information

**ABSTRACT:** In biominerals, proteins are key elements in the controlled nucleation and growth of the mineral phase. We report here on the coupled evolution of the organic and inorganic structures during the nucleation and growth of CaCO<sub>3</sub> under a monolayer of acidic  $\beta$ -sheet forming peptides that mimic the natural proteins found in nacre. The investigation is carried out using in situ analytical techniques (X-ray diffraction and IR spectroscopy) to provide molecular scale structural information over the whole course of the mineralization process. Mineralization is shown to coexist with  $\beta$ -sheet order while inducing other conformational changes to the peptide assembly. Peptides promote the growth of unoriented vaterite crystals; no templating effect of the  $\beta$ -sheet order is observed.



## INTRODUCTION

The field of biomineralization aims at understanding how organisms exert control over inorganic materials to build organic–inorganic functional structures such as bones, teeth, and shells. Specific proteins can control the location of the mineral nucleation, as well as the orientation, shape, and polymorph of the biogenic crystals.<sup>1–8</sup> In calcium carbonate bearing organisms (like mollusk shells), proteins found in association with the mineral share some common features:<sup>9</sup> they are rich in Ca<sup>2+</sup>-coordinating residues (Asp, Glu),<sup>10,11</sup> often present as repetitive sequences,<sup>12</sup> and they have been found in some studies to adopt a  $\beta$ -sheet secondary structure.<sup>3,6,13–15</sup>  $\beta$ -sheet forming acidic proteins are also associated with calcium phosphate structures<sup>16–18</sup> and were found to play an important role in the nucleation of this mineral.<sup>19</sup> Weiner et al.<sup>13</sup> have hypothesized that the regular array of carboxylic groups exposed within an acidic  $\beta$ -sheet might act as a template for the epitaxial growth of aragonite (a calcium carbonate polymorph) observed in pearl oyster shells.

This hypothesis has prompted a number of in vitro investigations of CaCO<sub>3</sub> formation in contact with  $\beta$ -sheet forming peptides either in bulk or as a Langmuir film to probe the influence of the secondary structure of the organic film on the mineral precipitation.<sup>20–24</sup> In bulk, all situations where  $\beta$ -sheet conformation was evidenced prior to mineralization were shown to promote oriented nucleation of calcite. At the air–water interface, adaptability, which is defined here as a possible deformation of the organic molecular lattice to adapt to the mineral lattice, was put forward as a key element of the templating by fatty acid monolayers.<sup>25,26</sup> This deformation was observed for  $\beta$ -sheet conformed monolayers<sup>24</sup> or hydrogen-bonded monolayers,<sup>27</sup> and here also only calcite crystals,

although exhibiting unusual growth habits, were observed. However, in all of these studies, no evidence was given of the stability of the organic structure during the crystal growth. Moreover, by using in situ techniques like grazing incidence X-ray surface diffraction (GIXD) on arachidic acid films, DiMasi et al. pointed out that kinetic effects could be more important than the templating effect in selecting polymorph and orientation.<sup>28</sup> The in situ follow-up of the mineralization events showed that the observed final orientation actually resulted from crystal rearrangements due to surface tension, and not from interactions of the mineral phase with the organic template. This went against former ex situ studies on the same system, which claimed that templating could select crystal orientation.<sup>29,30</sup> Loste et al.<sup>31</sup> reached the same conclusion by studying CaCO<sub>3</sub> growth under a series of fatty acid monolayers; Pouget et al.<sup>32</sup> have recently outlined the conditions under which either templating or kinetic effects can be dominant. For arachidyl sulfate monolayers films, however, GIXD revealed the epitaxial growth of CaCO<sub>3</sub> and the related mutual adaptation at the atomic scale of the organic and inorganic crystalline networks.<sup>33</sup>

In situ techniques like GIXD or IR reflectivity allow time-resolved studies of mineralization processes and provide information about both the mineral and the organic structures at the molecular scale. In this study, we provide space and time-resolved data of CaCO<sub>3</sub> nucleation and growth in contact with two different  $\beta$ -sheet peptide Langmuir monolayers that were selected as templates. In previous publications,<sup>34–36</sup> we have

Received: December 2, 2011

Revised: February 22, 2012

shown that the short amyloid-like peptide LSFDNSGAIITG-NH<sub>2</sub> (abbreviated as LSFDF), which exhibits a quasi-alternating sequence of hydrophobic and hydrophilic residues, forms 2D crystalline  $\beta$ -sheet arrays at the air–water interface, giving rise to characteristic grazing incidence X-ray diffraction peaks. This could be expected as this peptide adopts a similar conformation in bulk<sup>37</sup> and because alternating sequences of hydrophobic and hydrophilic residues are known to promote  $\beta$ -sheet ordering at the air–water interface.<sup>24,38,39</sup> LSFDF is only mildly acidic; a second oligopeptide was therefore designed, LDFDNSGDFDL-NH<sub>2</sub> (abbreviated as LDFDF), with the typical acid-residue content of proteins involved in nacre CaCO<sub>3</sub> formation ( $\sim 25$ –40% according to Weiner and Hood<sup>12</sup> or Samata<sup>40</sup>), and again with a quasi-alternating hydrophilic/hydrophobic sequence to promote  $\beta$ -sheet conformation. These two peptides represent simple promising model systems of CaCO<sub>3</sub> associated proteins: both self-assemble into flat  $\beta$ -sheet films (see below for LDFDF) at a hydrophilic/hydrophobic (water/air) interface, reminiscent of protein adsorption on the insoluble organic matrix of nacre,<sup>1,7</sup> and both exhibit a primary sequence short enough to allow numerical simulations.<sup>41</sup> Moreover, their comparison may provide new insights on the relative influence of conformation and charge density on the mineralization process. At last, their crystalline order in absence of minerals allows one to track very precisely the induced changes on organic conformation due to mineralization. Here, we show that the two peptides strongly promote an unstable polymorph, vaterite, while maintaining a  $\beta$ -sheet conformation. Vaterite is seen to grow without preferred orientation: this rules out pure templating effects and confirms the importance of kinetics at the interfacial nucleating layer.

## MATERIALS AND METHODS

**Peptides.** Peptides (purity >95%, net peptide content is 50% for LSFDF and 48.6% for LDFDF) were synthesized by Bachem (Switzerland). LSFDF was dissolved in hexafluoroisopropanol (HFIP) and then spread at the air–water interface in a Langmuir trough or Petri dish from a 1:6 HFIP:chloroform solution (peptide concentration: 0.02 g/L). LDFDF could only be dissolved in trifluoroacetic acid (TFA). It was then spread from a 1:10 TFA:chloroform solution on the water surface (peptide concentration: 0.015 g/L). As TFA is a strong acid, it lowers the subphase pH from pH 5.6 to 2.8 for water, and from 8.3 to 7.0 when using NaHCO<sub>3</sub> 10 mM, which acts as a buffer. This pH decrease was taken into account when performing the crystallization control experiments (see Figure 3).

**Mineralization Experiments.** Supersaturated solution was prepared by mixing equal volumes of 20 mM NaHCO<sub>3</sub> and 20 mM CaCl<sub>2</sub> to obtain 10 mM Ca(HCO<sub>3</sub>)<sub>2</sub>. The solution was poured in a Langmuir trough (Riegler & Kirstein, Germany), and the peptides were spread at the surface and compressed. Experiments in Langmuir trough were performed at 20 °C; experiments using Petri dishes were carried out at room temperature ( $\sim 20$  °C). Crystals grow preferentially at the interface due to the escape of gaseous CO<sub>2</sub>:  $2\text{HCO}_3^- + \text{Ca}^{2+} \rightarrow \text{CaCO}_3 + \text{H}_2\text{O} + \text{CO}_2$ .

**ATR-IR and IRRAS.** To get better statistics or to test the influence of pH, CO<sub>2</sub> escape rate, and peptide solvent (Supporting Information 4), multiple mineralization experiments were performed in Petri dishes of fixed area ( $\sim 60$  cm<sup>2</sup>) and analyzed by ATR-IR measurements. The quantity of spread peptide was adjusted to correspond to a surface pressure of  $\Pi = 10$  mN/m. These two methods yielded similar results in terms of polymorph and crystal morphology. Prior to ATR-IR analysis, the crystals were collected from the surface, washed with pure water, dried, and then pressed against the ATR diamond of an FTIR spectrometer (Bruker Optics) for spectra acquisition. We used the method described by Vagenas et al.<sup>42</sup> to extract the mass percentages

of the calcite–vaterite mixture from the IR spectrum in the 700–750 cm<sup>-1</sup> region (Supporting Information 4).

For IRRAS experiments, peptides were spread at the surface of a Langmuir trough (Riegler & Kirstein, Germany), under N<sub>2</sub> atmosphere, and compressed at a speed of 8.4 cm<sup>2</sup>/min. IRRAS measurements were performed at an incidence angle of 40°, with p-polarized light, at a resolution of 4 cm<sup>-1</sup>. A reference scan on a trough filled with ultrapure water was collected every time prior to sample scan.

**GIXD.** GIXD measurements were carried out at the beamline BW1 at HASYLAB (DESY, Hamburg, Germany). The monochromatic X-ray beam ( $\lambda = 1.304$  Å) impinged on the interface at an incidence angle  $\alpha_i = 0.85\alpha_c$ , where  $\alpha_c$  (0.13°) is the critical angle for total reflection of the X-ray beam on the water surface. The size of the beam footprint is  $\sim 2 \times 50$  mm<sup>2</sup>. The scattered intensity was detected by a vertical linear Mythen detector module (PSI, Switzerland) with 1280 strips designed for time-resolved powder diffraction experiments. The detector was rotated to scan  $q_{xy}$  in-plane scattering values. The out-of-plane  $q_z$  component of the scattering vector was detected in the range  $0.0 \text{ \AA}^{-1} \leq q_z \leq 0.8 \text{ \AA}^{-1}$ . The  $q_{xy}$  positions of the Bragg peaks yield the lattice repeat distances  $d = 2\pi/q_{xy}$  of the interfacial ordered structures. The coherence length  $L_{xy}$ , a measure of the range of the crystalline order, can be inferred from the full-width at half-maximum (fwhm) of the Bragg peaks according to  $L_{xy} = 0.9(2\pi)/\text{fwhm}(q_{xy})$ . The in-plane resolution ( $\sim 0.1^\circ$ ) was defined by a Soller slit collimation.

## RESULTS

We first probed the molecular organization of a compressed LDFDF monolayer at the air–water interface by GIXD measurements. Like the LSFDF peptide film, the LDFDF film shows X-ray diffraction peaks typical of a 2D crystalline  $\beta$ -sheet order (see Figure 1 for surface pressure  $\pi = 10$  mN/m and pH = 2.8).

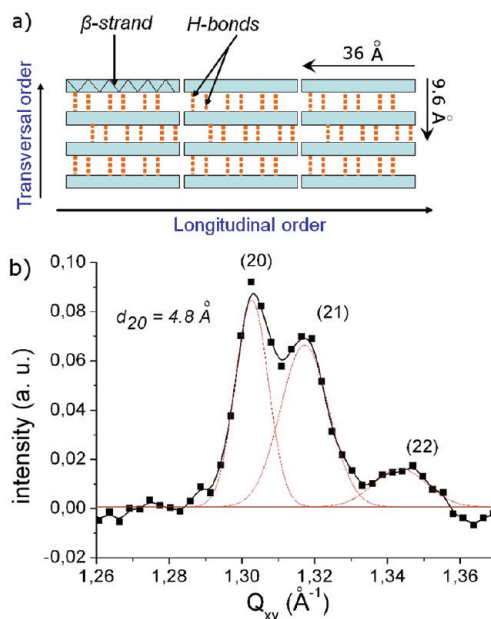


**Figure 1.** (a) LSFDF and LDFDF form a 2D molecular array at the air–water interface: hydrogen bonding gives rise to a transverse order, with interstrand distances ( $\sim 4.8$  Å) characteristic of a  $\beta$ -sheet arrangement, while peptide end-group interactions are responsible for the longitudinal ordering of the peptides, along their backbone. Both orders translate into GIXD diffraction peaks, shown in (b) for the transverse order of a LDFDF monolayer at a surface pressure of 10 mN/m on water, pH 2.8. Deconvolution and indexing of the peaks follows the method applied previously to LSFDF.<sup>35</sup>

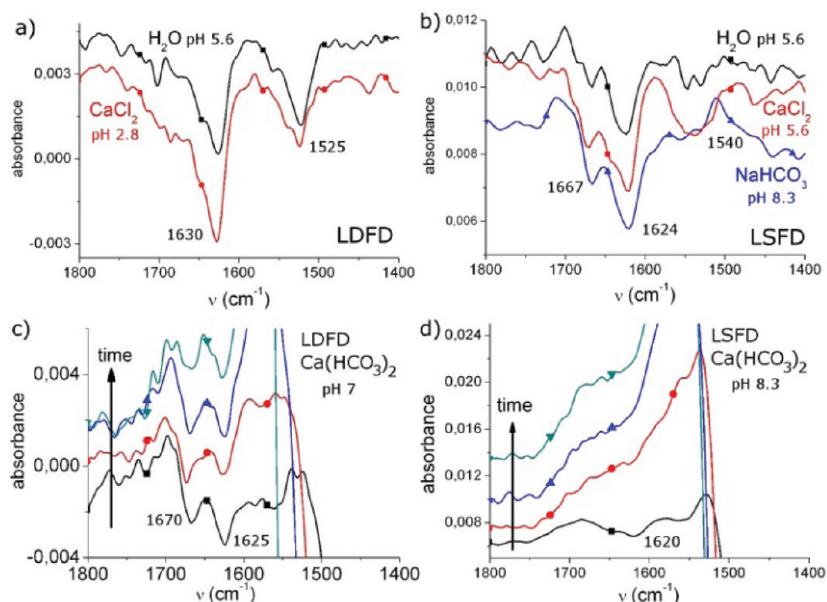


**Figure 2.** Reflection-absorption spectra ( $A = -\log(I/I_0)$  with  $I$  and  $I_0$  are the reflected intensities of the sample and of the reference trough respectively) of the Amide I and II regions of LDFD and LSFd monolayers on different solutions at 10 mN/m. The absorption bands point downwards because the reflected intensity is measured, instead of the transmitted one. On non-mineralizing subphases (a–b) both peptides show a marked peak at 1625–1630  $\text{cm}^{-1}$  characteristic of  $\beta$ -sheet conformation; LSFd also exhibits some  $\beta$ -turns (1670  $\text{cm}^{-1}$ ). (c–d) Evolution of the Amide I and II bands on  $\text{Ca}(\text{HCO}_3)_2$  at times 30, 65, 90, 340 min (LDFD) and 10, 30, 75, 330 min (LSFD) after monolayer formation. The sharp dip of the absorbance around 1500  $\text{cm}^{-1}$  is due to the asymmetrical  $\text{CO}_3^{2-}$  stretching band (1420–1500  $\text{cm}^{-1}$ ) of the growing vaterite. On  $\text{Ca}(\text{HCO}_3)_2$ , LDFD presents a mixed  $\beta$ -turn/ $\beta$ -sheet conformation which is stable over time. For LSFd, the amide I and amide A (SI.3) bands were seen to fade away within  $\sim 1$  h after monolayer formation. Since LSFd is stable at pH 8.3 or in the presence of  $\text{Ca}^{2+}$  (b) this fading is probably due to peptide adsorption on  $\text{CaCO}_3$  crystals.

Bragg peaks can be indexed using a rectangular unit cell of parameters  $a = 9.6 \text{ \AA}$  and  $b = 36 \text{ \AA}$ . The in-plane (20) peak (see Figure 1b) corresponds to a repeat distance of 4.8  $\text{\AA}$ , which is the typical interstrand distance defined by the hydrogen-bond network in a  $\beta$ -sheet conformation. Another series of peaks (not shown) at lower  $Q_{xy}$ , centered around  $Q_z = 0$  (no out-of-plane component), is associated with peptide ordering along the peptidic backbone. The repeat distance along this crystalline axis is  $b = 36 \text{ \AA}$  at  $\pi = 10 \text{ mN/m}$ , which almost coincides with the length of the peptide in a fully extended configuration ( $11 \times 3.45 = 37.95 \text{ \AA}$ ). This result indicates that like the LSFd peptide, LDFD is able to form  $\beta$ -sheet films lying flat at the air–water interface, with crystalline domains about 150 nm large ( $\sim 300$  peptides) along the hydrogen-bond network and about 100 nm ( $\sim 20$ – $25$  peptides) along the peptidic backbone.

LSFD and LDFD form stable monolayers (see Langmuir isotherms and AFM pictures in the Supporting Information 1–2) on  $\text{H}_2\text{O}$ ,  $\text{CaCl}_2$  solutions, and a supersaturated  $\text{CaCO}_3$  solution that we denote  $\text{Ca}(\text{HCO}_3)_2$ . For LDFD, no surface pressure rise was observed on  $\text{NaHCO}_3$  solution at pH 7 (see Materials and Methods for an explanation of the different pH values), indicating that the monolayer is unstable at this pH value and that  $\text{Ca}^{2+}$  ions are responsible for the observed stabilization of LDFD on  $\text{Ca}(\text{HCO}_3)_2$  at pH 7. Similar behavior has been observed for arachidyl sulfate monolayers, which are soluble in the absence of  $\text{Ca}^{2+}$  ions.<sup>33</sup> For all stable monolayers, IRRAS spectra (see Materials and Methods) exhibit a peak at 1625  $\text{cm}^{-1}$  characteristic of a  $\beta$ -sheet secondary structure<sup>43</sup> (Figure 2a,b).

On  $\text{Ca}(\text{HCO}_3)_2$ , LDFD monolayer remains stable as mineralization proceeds and exhibits a band at  $1671 \pm 3$

$\text{cm}^{-1}$  (Figure 2c) characteristic of  $\beta$ -turns, presumably induced by the binding of  $\text{Ca}^{2+}$  ions to deprotonated aspartic acids. For LSFd on  $\text{Ca}(\text{HCO}_3)_2$ , the peak at 1625  $\text{cm}^{-1}$  (Figure 2d) as well as the amide A band (Supporting Information 3) fade away gradually within 1 h after monolayer formation, indicating that the peptide desorbs from the interface. The attenuation length of the IR beam at 3300  $\text{cm}^{-1}$  (amide A band) in water is only  $\sim 1 \mu\text{m}$ , on the order of the  $\text{CaCO}_3$  crystal size after  $\sim 1$  h of growth. Adsorption of the peptides on nascent  $\text{CaCO}_3$  crystals and subsequent displacement of the peptides from the air–water interface due to crystal growth could therefore explain why the amide A band is seen to disappear. Alternatively, the combination of  $\text{Ca}^{2+}$  chelation with increased pH could enhance the bulk solubility of LSFd and also lead to desorption.

When observed with the naked eye,  $\text{CaCO}_3$  crystals grown under peptide monolayers form a thin uniform white film at the air–water interface. Crystals were found mostly in those parts of the Langmuir trough where peptide was present (very few or no crystals could be seen in the area devoid of peptides, on the other side of the compression barriers), indicating that the peptides promote  $\text{CaCO}_3$  nucleation as compared to a bare interface. Optical microscopy pictures (Figure 3a–c) indicate that the two main polymorphs found are calcite (rhombohedral) and vaterite (florete-like morphology).

Mass percentages of the different polymorphs deduced from ATR-IR measurements (see Figure 3d and Supporting Information 4) indicate that LDFD (10 mN/m) yielded  $99 \pm 0.5\%$  vaterite versus  $4 \pm 5\%$  vaterite for the control experiment without monolayer (at pH 7). LSFd (10 mN/m) yielded  $85 \pm 2\%$  vaterite versus  $27 \pm 1\%$  for the control experiment (at pH 8.3). Increasing the gas escape rate or pH

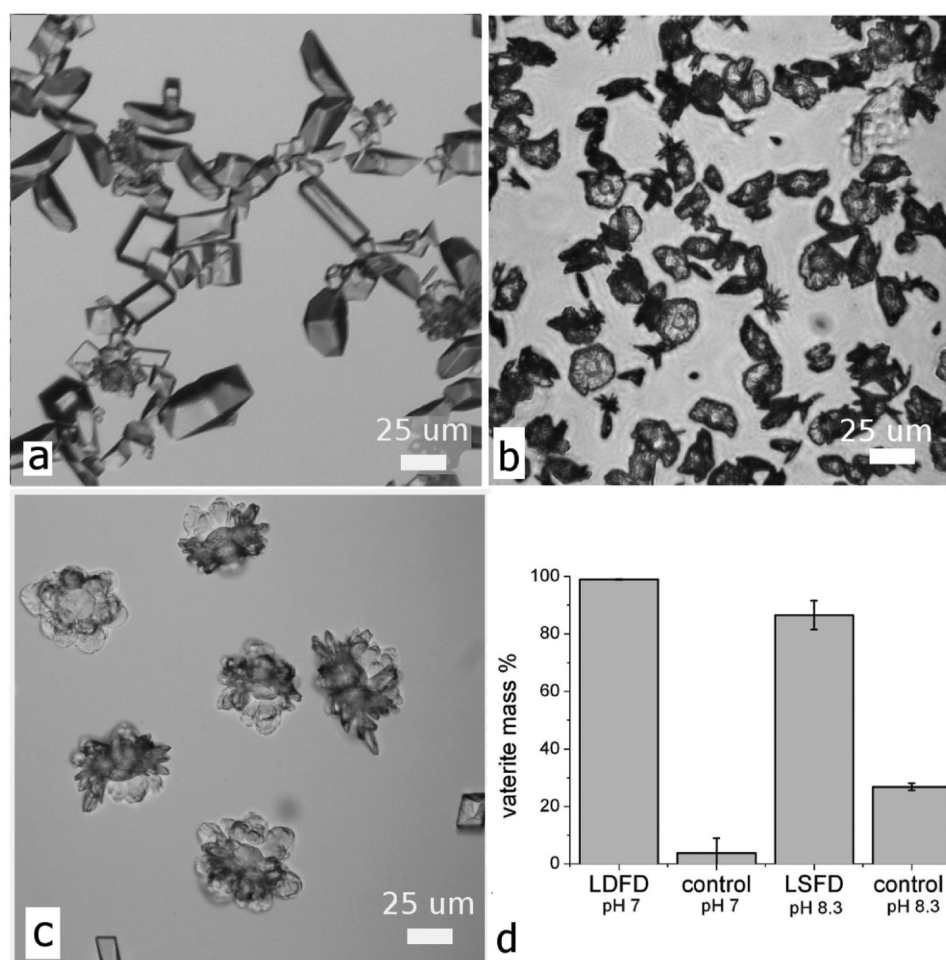


**Figure 3.** Representative optical microscopy pictures of the interfacial  $\text{CaCO}_3$  crystals obtained after 16 h-growth from a 10 mM  $\text{Ca}(\text{HCO}_3)_2$  solution (a) without monolayer, (b) under LDFD at 10 mN/m, and (c) under LSFD at 10 mN/m. (a) and (c) were taken directly at the air–water interface, while (b) was taken after transfer of the crystals on a glass slide. (d) Mass percentages of vaterite obtained from ATR-IR spectra (see Materials and Methods) for each case, averaged over two separate growth experiments performed under identical conditions.

(in the range 6.5–9) also results in an increased vaterite content (Supporting Information 4), but never to the extent of that obtained with the peptides. This precludes any dominant effect of possible pH modification at the interface. The promotion of vaterite formation by the peptide film was further confirmed in separate experiments by GIXD (see below) and IRRAS measurements (Supporting Information 5). To understand why the peptide films selectively nucleate vaterite, and to unravel possible templating mechanisms, we used GIXD to monitor simultaneously the structure of the organic monolayer and the  $\text{CaCO}_3$  nucleation at the nanometer length scale. Time-resolved ( $Q_y, Q_z$ ) maps are shown in Figure 4.

Calcite (diffraction spots) and vaterite (rings) appear simultaneously (time resolution: 30 min) in all experiments, although calcite spots are scarce under LDFD and LSFD, in qualitative agreement with the ATR-IR results (Figure 3d). The continuous diffraction rings, and the fact that their relative intensities closely follow that of the powder diffraction pattern, indicate that vaterite nucleates as a 3D powder at the air–water interface. Coherence lengths (see Materials and Methods for calculation formula) of the vaterite crystals evolve over time from  $\sim 15$  to 30 nm. On the contrary, the discrete diffraction

spots originate from calcite crystals presenting selected orientations with respect to the interface.

On  $\text{Ca}(\text{HCO}_3)_2$ , the peptide monolayer gives rise to a single diffraction peak at 4.83 Å (LDFD) and 4.8 Å (LSFD), corresponding to the  $\beta$ -sheet interstrand distance. The interstrand distance remains constant in time for both peptides (Figure 5a).

For LSFD, the integrated intensity of this diffraction peak monotonously decreases, while it remains constant for LDFD (Figure 5b), in agreement with the IRRAS measurements. Unlike on water, no order along the peptide backbone (longitudinal order) is present for both peptides.

## DISCUSSION

The two model peptides LSFD and LDFD were selected to probe the templating influence of the  $\beta$ -sheet conformation on crystalline calcium carbonate formation. In this study, we chose to use model peptides rather than specific proteins extracted from biominerals for two reasons. First, the simpler and shorter structure of our peptides enables us to clearly follow modifications in the organic conformation. In particular, both LSFD and LDFD present a strong bidimensional crystalline order, a good starting point to probe conformational changes and adaptability. Second, their short sequence allows numerical

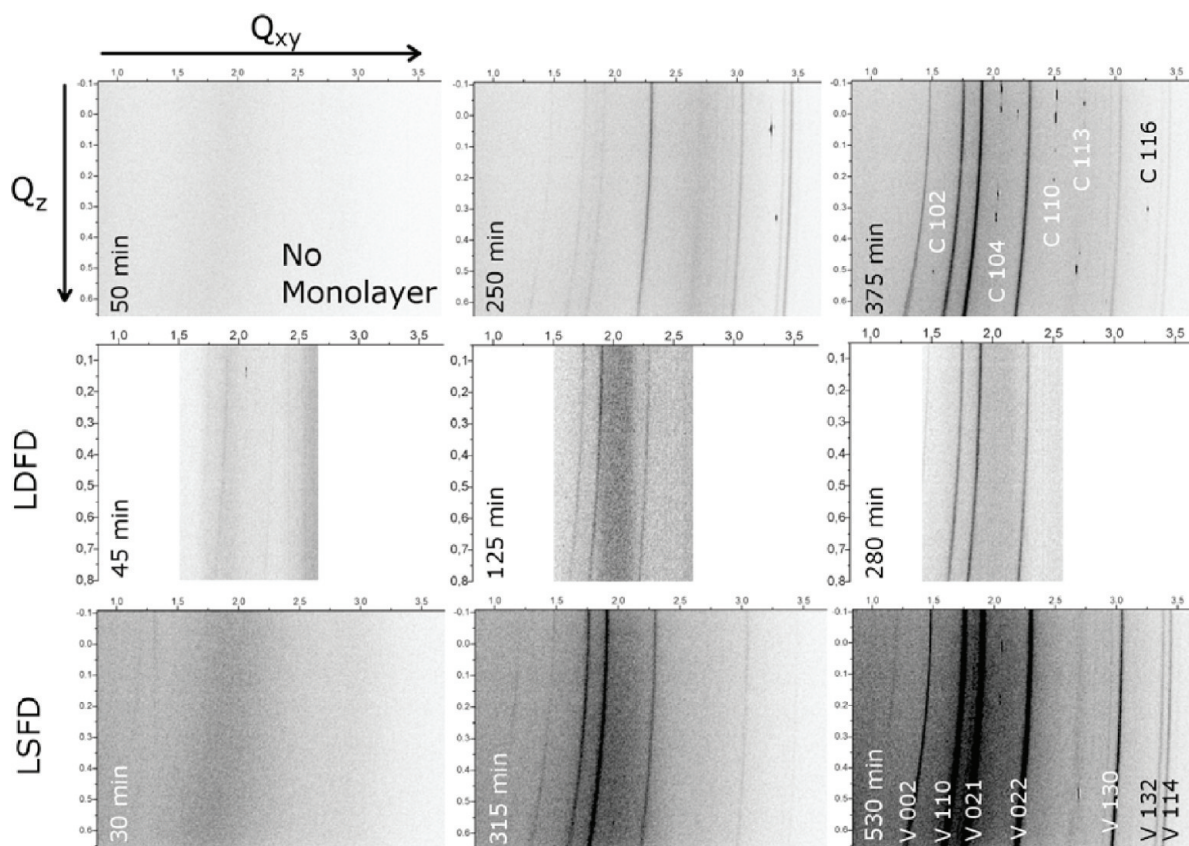


**Figure 4.** GIXD ( $Q_{xy}$ ,  $Q_z$ ) maps of 10 mM  $\text{Ca}(\text{HCO}_3)_2$  solutions without monolayer, with LDFD, and with LSFDF. The time shown is the one elapsed since the mixing of  $\text{CaCl}_2$  and  $\text{NaHCO}_3$  solutions. The indexing of the continuous diffraction rings (vaterite) or of the discrete diffraction spots (calcite) present in all pictures is shown in only two selected frames for the sake of clarity.

simulations to be performed (work under progress). Both selected peptides exhibit similar lengths (11 or 12 aminoacids) but a different acidity and therefore charge density.

Both peptides show structural changes when interacting with mineralizing calcium carbonate as they both lose their crystalline longitudinal order while keeping a  $\beta$ -sheet conformation, with a constant-in-time interstrand distance.  $\beta$ -turns appear in the LDFD conformation, while LSFDF seems to undergo a progressive desorption. A parallel can be drawn between the loss of crystalline longitudinal order observed here and the experiments conducted by DiMasi et al.<sup>44</sup> and Popescu et al.<sup>27</sup> on valine-based bis-urea surfactants: in their investigations, addition of  $\text{Ca}^{2+}$  ions in the subphase induced a loss of ordering along the direction perpendicular to the H-bonding. This is similar to what is observed in the case of a LDFD monolayer on  $\text{CaCl}_2$  at pH 5.6. However, in the case of a LSFDF monolayer, the longitudinal order is strong enough to resist the addition of  $\text{CaCl}_2$  at pH = 5.6 and only disappears on a mineralizing  $\text{Ca}(\text{HCO}_3)_2$  subphase.

Both peptides strongly favor the selection of the unstable polymorph vaterite (85–99% mass percentage of vaterite, while precipitation without monolayer generated no more than 45% vaterite for all conditions used; see Supporting Information 4). Although unoriented vaterite is sometimes listed as being one of the produced  $\text{CaCO}_3$  polymorphs,<sup>30,45</sup> such a high measured selectivity has only been obtained in a few studies.<sup>32</sup> The GIXD spectra of vaterite grown under peptide films are identical to those of the  $\sim 20\%$  vaterite found in the control experiment without peptide (although kinetics are much slower in this latter case). In particular, vaterite is not oriented, precluding

any epitaxial templating effects. It is known that  $\text{CaCO}_3$  can nucleate from a supersaturated solution first as the more soluble vaterite and then transform to calcite<sup>46–49</sup> following Ostwald's empirical rule of stages (although evidence of this rule is less well documented under monolayers). Polymorph-sensitive IRRAS measurements (Supporting Information 5) performed without monolayer could not, however, show that the formation of calcite first proceeds through a vaterite precursor, implying that, if such a transformation does take place, its kinetics is faster than the time resolution of our IRRAS measurements ( $\sim 5$  min). Pichon et al.<sup>49</sup> indeed showed by TEM that a sequential amorphous–vaterite–calcite transformation takes place within  $\sim 5$  min for  $\text{CaCO}_3$  growth under valine-based bis-urea surfactants. It is therefore possible that the peptides used here could act as inhibitors of the vaterite-to-calcite transformation. Alternatively, they could also favor vaterite nucleation by charge density effects as those invoked by Fricke et al.<sup>45</sup>

Our results differ markedly from those of Cavalli et al.<sup>24</sup> who showed that a  $\beta$ -sheet array could act as an efficient template to produce oriented calcite. It should be noted that the mineralization technique used in their study (Kitano's method) is different from ours (salt mixing): different kinetic pathways may explain the observed different influence of the peptidic film on mineralization. Also, peptide sequences and the influence of  $\text{Ca}^{2+}$  ions on the isotherms of the surfactant molecules are different, all of which could strongly influence the obtained polymorph. It should finally be noted that the peptides used did not nucleate any aragonite, indicating that a simple  $\beta$ -sheet order along one direction is not sufficient to favor the

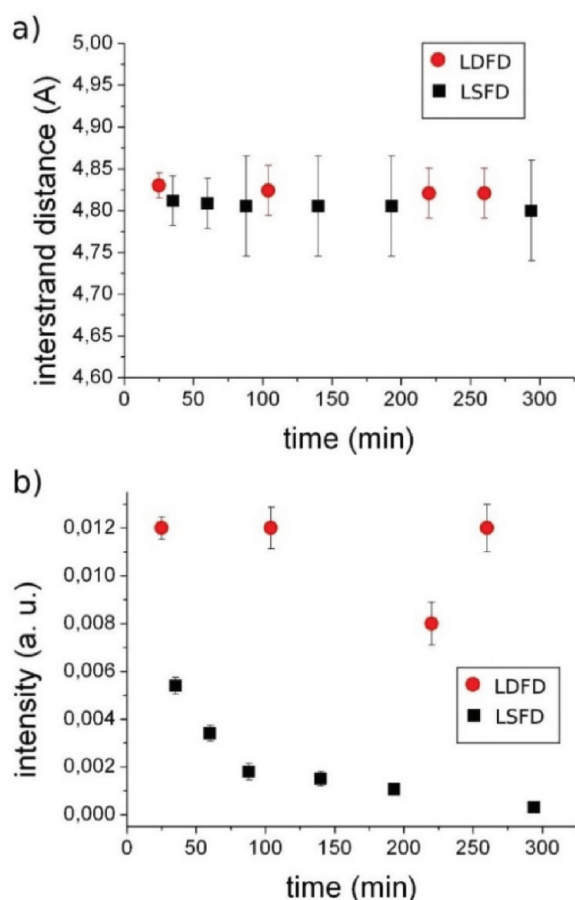


**Figure 5.** (a)  $\beta$ -sheet interstrand distance derived from diffraction peak (20) and (b) integrated intensity of the transverse order diffraction peak (20), both of LDFD and of LSFD, as a function of the time elapsed since monolayer formation on  $\text{Ca}(\text{HCO}_3)_2$ . Error bars in (a) are due primarily to the  $\Delta Q_y$  step selected for each scan, while those in (b) are uncertainties of the Gaussian fit of the diffraction peak.

formation of this polymorph. Very few studies have so far succeeded in demonstrating aragonite selection by monolayers;<sup>6,20,50</sup> in vivo, selection of this polymorph requires highly specialized proteins as shown recently.<sup>10</sup>

## CONCLUSION

A pure  $\beta$ -sheet arrangement is not enough to provide the conditions for a templating effect and induce the oriented growth of crystalline  $\text{CaCO}_3$  polymorphs like those found in mollusk shells. Comparing our investigations to other studies of  $\text{CaCO}_3$  growth under  $\beta$ -sheet or H-bond ordered monolayers,<sup>24,27,44</sup> it seems possible that a lack of flexibility, that is, the ability of the side group to rearrange and adapt their organization in response to the mineral phase, of the peptides used here might explain why no orientational templating effect was observed. No specific organic/inorganic interactions could be evidenced in our study; the peptidic film did however exert an influence on polymorph and kinetics as it was shown to induce almost pure vaterite production, either by enhancing its nucleation rate or by kinetic stabilization of this thermodynamically unstable polymorph. This resembles recently reported results on  $\text{CaCO}_3$  growing under lipid monolayers.<sup>47</sup>

We believe that the experimental methodology developed in this work can provide unique insights on biomineralization, as time and space-resolved data at the molecular level are essential

to understand the protein–mineral interactions that drive the biomineralization process. In the future, we therefore plan to apply this methodology to more complex model systems involving either polymer additives like poly(acrylic acid) or full protein extracts of biominerals. The use of polymer additives in the subphase should in particular favor the initial formation of an amorphous  $\text{CaCO}_3$  phase<sup>51–53</sup> and thus drastically change the kinetic route to a crystalline polymorph.

## ASSOCIATED CONTENT

### Supporting Information

(1) Isotherms of peptides on different subphase solutions; (2) AFM study of LDFD film morphology; (3) amide A IRRAS bands of peptide films; (4) ATR-IR spectra of  $\text{CaCO}_3$ , influence of pH, and degassing rate; and (5) IRRAS spectra of  $\text{CaCO}_3$  growth. This material is available free of charge via the Internet at <http://pubs.acs.org>.

## AUTHOR INFORMATION

### Corresponding Author

\*Tel.: (+) 33 1 69 08 74 33. Fax: (+) 33 1 69 08 66 40. E-mail: [patrick.guenoun@cea.fr](mailto:patrick.guenoun@cea.fr).

### Notes

The authors declare no competing financial interest.

## ACKNOWLEDGMENTS

We acknowledge the use of HASYLAB (Hamburg, Germany) BW1 beamline and thank B. Struth for technical help. We also thank the RTRA “Triangle de la Physique” for its financial help regarding the IRRAS equipment (IRMA project).

## REFERENCES

- (1) Mann, S. *Bioinorganic Chemistry: Principles and Concepts in Bioinorganic Chemistry*; O. U. Press, Oxford Chemistry Masters: Oxford, 2001.
- (2) Nudelman, F.; Gotliv, B.; Addadi, L.; Weiner, S. *J. Struct. Biol.* **2006**, *153*, 176–187.
- (3) Weiner, S.; Talmon, Y.; Traub, W. *Int. J. Biol. Macromol.* **1983**, *5*, 325–328.
- (4) Donnay, G.; Pawson, D. *Science* **1969**, *166*, 1147.
- (5) Aizenberg, J.; Tkachenko, A.; Weiner, S.; Addadi, L.; Hendler, G. *Nature* **2001**, *412*, 819–822.
- (6) Falini, G.; Albeck, S.; Weiner, S.; Addadi, L. *Science* **1996**, *271*, 67–69.
- (7) Lowenstam, H.; Weiner, S. *On Biomineralization*; Oxford University Press: New York, 1989.
- (8) Currey, J. D. *Bones: Structure and Mechanics*; Princeton University Press: NJ, 2006.
- (9) Evans, J. *Curr. Opin. Colloid Interface Sci.* **2003**, *8*, 48–54.
- (10) Suzuki, M.; Saruwatari, K.; Kogure, T.; Yamamoto, Y.; Nishimura, T.; Kato, T.; Nagasawa, H. *Science* **2009**, *325*, 1388–1390.
- (11) Dauphin, Y.; Cuif, J. *Electrophoresis* **1997**, *18*, 1180–1183.
- (12) Weiner, S.; Hood, L. *Science* **1975**, *190*, 987–988.
- (13) Weiner, S.; Traub, W. *FEBS Lett.* **1980**, *111*, 311–316.
- (14) Worms, D.; Weiner, S. *J. Exp. Zool.* **1986**, *237*, 11–20.
- (15) Fu, G.; Qiu, S.; Orme, C.; Morse, D.; De Yoreo, J. *Adv. Mater.* **2005**, *17*, 2678.
- (16) Lee, S.; Veis, A.; Glonek, T. *Biochemistry* **1977**, *16*, 2971–2979.
- (17) Renugopalakrishnan, V.; Uchiyama, A.; Horowitz, P.; Rapaka, R.; Suzuki, M.; Lefteriou, B.; Glimcher, M. *Calcif. Tissue Int.* **1986**, *39*, 166–170.
- (18) He, G.; Dahl, T.; Veis, A.; George, A. *Nat. Mater.* **2003**, *2*, 552–558.

- (19) Takeuchi, A.; Ohtsuki, C.; Kamitakahara, M.; Ogata, S.-i.; Miyazaki, T.; Tanihara, M. *J. Mater. Sci.: Mater. Med.* **2008**, *19*, 387–393.
- (20) Levi, Y.; Albeck, S.; Brack, A.; Weiner, S.; Addadi, L. *Chem.-Eur. J.* **1998**, *4*, 3.
- (21) Addadi, L.; Moradian, J.; Shay, E.; Maroudas, N.; Weiner, S. *Proc. Natl. Acad. Sci. U.S.A.* **1987**, *84*, 2732.
- (22) Volkmer, D.; Fricke, M.; Huber, T.; N, S. *Chem. Commun.* **2004**, 1872.
- (23) Addadi, L.; Weiner, S. *Proc. Natl. Acad. Sci. U.S.A.* **1985**, *82*, 4110–4114.
- (24) Cavalli, S.; Popescu, D.; Tellers, E.; Vos, M.; Pichon, B.; Overhand, M.; Rapaport, H.; Sommerdijk, N.; Kros, A. *Angew. Chem., Int. Ed.* **2006**, *45*, 739–744.
- (25) Ahn, D.; Berman, A.; Charych, D. *J. Phys. Chem.* **1996**, *100*, 12455.
- (26) Berman, A.; Ahn, D.; Lio, A.; Salmeron, M.; Reichert, A.; Charych, D. *Science* **1995**, *269*, 515–518.
- (27) Popescu, D. C.; Smulders, M. M. J.; Pichon, B. P.; Chebotareva, N.; Kwak, S.-Y.; van Asselen, O. L. J.; Sijbesma, R. P.; DiMasi, E.; Sommerdijk, N. A. J. M. *J. Am. Chem. Soc.* **2007**, *129*, 14058–14067.
- (28) DiMasi, E.; Olszta, M.; Patel, V.; Gower, L. *CrystEngComm* **2003**, *5*, 346–350.
- (29) Rajam, S.; Heywood, B.; JBA, W.; Mann, S. *J. Chem. Soc., Faraday Trans.* **1991**, *87*, 727.
- (30) Mann, S.; Heywood, B.; Rajam, S.; Birchall, J. *Nature* **1988**, *334*, 692–695.
- (31) Loste, E.; Diaz-Marti, E.; Zorbakhsh, A.; Meldrum, F. *Langmuir* **2003**, *19*, 2830–2837.
- (32) Pouget, E. M.; Bomans, P. H. H.; Goos, J. A. C. M.; Frederik, P. M.; de With, G.; Sommerdijk, N. A. J. M. *Science* **2009**, *323*, 1455–1458.
- (33) Kewalramani, S.; Kim, K.; Stripe, B.; Evmenenko, G.; Dommett, G. H. B.; Dutta, P. *Langmuir* **2008**, *24*, 10579–10582.
- (34) Lepère, M. Dissertation, UPMC, 2007.
- (35) Lepère, M.; Chevillard, C.; Brezesinski, G.; Goldmann, M.; Guenoun, P. *Angew. Chem., Int. Ed.* **2009**, *48*, 5005–5009.
- (36) Lepère, M.; Chevillard, C.; Hernandez, J.-F.; Mitraki, A.; Guenoun, P. *Langmuir* **2007**, *23*, 8150–8155.
- (37) Papanikolopoulou, K.; Schoehn, G.; Forge, V.; Forsyth, T.; Riekel, C.; Hernandez, J.; Ruigrok, R.; Mitraki, A. *J. Biol. Chem.* **2005**, *280*, 2481–2490.
- (38) Xu, G.; Wang, W.; Groves, J.; Hecht, M. *Proc. Natl. Acad. Sci. U.S.A.* **2001**, *98*, 3652–3657.
- (39) Rapaport, H.; Kjaer, K.; Jensen, T.; Leiserowitz, L.; Tirrell, D. J. *Am. Chem. Soc.* **2000**, *122*, 12523–12529.
- (40) Samata, T. *The Veliger* **1990**, *33*, 191.
- (41) Knecht, V. *J. Phys. Chem. B* **2008**, *112*, 9476–9483.
- (42) Vagenas, N.; Gatsouli, A.; Kontoyannis, C. *Talanta* **2003**, *59*, 831–836.
- (43) Barth, A.; Zscherp, C. *Q. Rev. Biophys.* **2002**, *35*, 369–430.
- (44) DiMasi, E.; Kwak, S.-Y.; Pichon, B. P.; Sommerdijk, N. A. J. M. *CrystEngComm* **2007**, *9*, 1192–1204.
- (45) Fricke, M.; Volkmer, D.; Krill, I. C.; Kellermann, M.; Hirsch, A. *Cryst. Growth Des.* **2006**, *6*, 1120.
- (46) Brecevic, L.; NothigLaslo, V.; Kralj, D.; Popovic, S. *J. Chem. Soc., Faraday Trans.* **1996**, *92*, 1017–1022.
- (47) Xiao, J.; Wang, Z.; Tang, Y.; Yang, S. *Langmuir* **2010**, *26*, 4977–4983.
- (48) Andreassen, J. *J. Cryst. Growth* **2005**, *274*, 256–264.
- (49) Pichon, B.; Bomans, P.; Frederik, P.; Sommerdijk, N. J. *Am. Chem. Soc.* **2008**, *130*, 4034–4040.
- (50) Litvin, A.; Valiyaveetil, S.; Kaplan, D.; Mann, S. *Adv. Mater.* **1997**, *9*, 124–127.
- (51) DiMasi, E.; Patel, V.; Sivakumar, M.; Olszta, M.; Yang, Y.; Gower, L. *Langmuir* **2002**, *18*, 8902–8909.
- (52) Gower, L.; Odom, D. *J. Cryst. Growth* **2000**, *210*, 719.
- (53) Pecher, J.; Guenoun, P.; Chevillard, C. *Cryst. Growth Des.* **2009**, *9*, 1306–1311.